

Universal inverse electrocaloric effect in perovskites

Xingyue Ma,^{1,2} Mingxing Chen,³ Jun-Ming Liu,¹ Di Wu,^{1,2,*} and Yurong Yang^{1,2,†}

¹National Laboratory of Solid State Microstructures and Collaborative Innovation Center of Advanced Microstructures, Nanjing University, Nanjing 210093, China

²Jiangsu Key Laboratory of Artificial Functional Materials, Department of Materials Science and Engineering, Nanjing University, Nanjing 210093, China

³School of Physics and Electronics, Hunan Normal University, Key Laboratory for Matter Microstructure and Function of Hunan Province, Key Laboratory of Low-Dimensional Quantum Structures and Quantum Control of Ministry of Education, Changsha 410081, People's Republic of China

 (Received 16 February 2023; revised 24 April 2023; accepted 27 April 2023; published 10 May 2023)

The electrocaloric effect (ECE) offers a promising alternative to the traditional gas compressing refrigeration due to its high efficiency and environmental friendliness. The unusual inverse (negative) electrocaloric effect refers to the adiabatic temperature drops due to the application of electric field, in contrast with the normal (positive) ECE, and provides ways to reach a larger temperature span in refrigeration cycles by combining the normal and inverse ECE. However, the inverse ECE is unusual and requires a clear understanding of microscopic mechanisms. Here, we found the unexpected and extensive inverse ECE in nonpolar orthorhombic, tetragonal, and cubic phases of halide and oxide perovskite at a wide temperature range by means of first-principle-based large-scale Monte Carlo methods. Such an unexpected inverse ECE originates from the octahedral tilting related entropy change rather than the polarization entropy change under the application of electric field. Furthermore, a giant inverse ECE with temperature change of 8.6 K is found at room temperature. This giant and extensive inverse ECE in perovskite opens up a new horizon in the research of caloric effects and broadens the electrocaloric refrigeration ways with high efficiency.

DOI: [10.1103/PhysRevB.107.184105](https://doi.org/10.1103/PhysRevB.107.184105)

I. INTRODUCTION

Refrigeration consumes energy intensively and more than 20% of the electricity generated in the world is used for cooling [1]. Solid state cooling technologies based on the caloric effects display an attractive alternative to the traditional vapor compression cycles due to the higher operating efficiency and zero greenhouse gas emission [2–4]. Caloric effects are the phenomena of temperature and entropy change induced by electric field [electrocaloric (EC)] [5–7], magnetic field (magnetocaloric) [8], mechanical stresses (elastocaloric [9], barocaloric [10], and twistocaloric [11]). EC based cooling technology is promising in modern microelectronics where millions of electronic units integration to the chip lead to tremendous power dissipation density and high-efficient thermal manage systems is highly required [12,13]. EC effects can be normal (or positive, where the entropy decreases and temperature increases with the application of electric field), and inverse (or negative, where the entropy increases and the temperature decreases with the application of electric field), as shown in Fig. 1. Both of the two EC effects can be used in cooling technologies [2,14]. Combining the normal and inverse electrocaloric effect (ECE) is proposed to enlarge the EC temperature span and optimize EC cooling cycles. [14–19].

Though the normal ECE have been intensively studied in single crystals [20], thin films [21], ceramic multilayer chips [22,23], polymer [6,24,25], and ceramic/polymer composite [26,27], the inverse ECE is found only in a few materials, basically complex polar relaxor and antiferroelectric oxides [15,28–32]. The presenting temperature and magnitude of negative EC coefficient are limited, and its microscopic mechanism is highly required to be revealed.

In addition to oxide perovskites, halide perovskites are also promising candidate materials in cost-effective, high-performance electronics and optoelectronics [33–35]. The temperature change under electric-field will give great impact on performance, degradation and reliability of the materials and devices. However, the response under electric field in halide perovskite and related materials is little studied.

Here, we investigated the EC effect in nonpolar halide (CsPbI₃) and oxide (BaCeO₃) perovskite using first-principles-based large-scale Monte Carlo (MC) simulation methods. Perovskite CsPbI₃ and BaCeO₃ can adopt nonpolar structures of orthorhombic, tetragonal, and cubic phases above room temperature. All the nonpolar phases possess the inverse ECE at small electric field. The giant inverse ECE with the temperature change –8.6 K under the field of 2.0 MV/cm at room temperature is found, which is comparable to the typically reported normal ECE with temperature change of +5.5 K under the field of 0.29 MV/cm near room temperature [22] or the inverse ECE with temperature change of –5.76 K under the field of 0.338 MV/cm at 59 °C [28].

*diwu@nju.edu.cn

†yangyr@nju.edu.cn

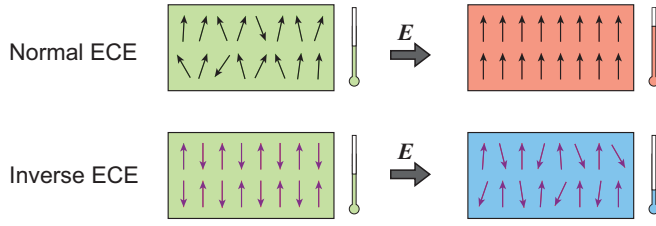


FIG. 1. Schematics of normal and inverse ECE. The top and bottom panels represent the normal and inverse ECE, respectively. The arrows in top and bottom panels correspond to local electric dipole and local antiferrodistortive (AFD) octahedral rotation vector, respectively. Note that both ordered AFD motion at low temperature (as shown here) and local disordered AFD motion at high temperature (which is instantaneous fluctuation with vanishing average value) could contribute to the inverse ECE.

This large and extensive inverse ECE comes from the entropy change related to octahedral antiferrodistortive (AFD) motion, both ordered motion at low temperature [see Fig. 2(a)] or disordered local motion at high temperature (which is instantaneous fluctuation with vanishing average value), and the strong coupling between AFD and polar motions.

This paper is organized as follows. In Sec. II, we describe the effective Hamiltonian, hybrid Monte Carlo simulation and phenomenological model used in this work. The inverse ECE in halide perovskite CsPbI₃ is described and analyzed in Sec. III in detail. Section IV gives a brief discussion. Finally, Sec. V summarizes this work.

II. METHODS

A. Effective Hamiltonian

We use the effective Hamiltonian methods developed in Ref. [36], along with the parameters computed from first-principle calculations. The degrees of freedom of effective Hamiltonian are local soft mode vectors $\{\mathbf{u}_i\}$ of each five-atom unit cell, local displacement vectors $\{\mathbf{v}_i\}$ related to inhomogeneous strain, pseudovectors $\{\boldsymbol{\omega}_i\}$ representing the rotation

of iodine octahedra [also known as antiferrodistortive (AFD) motions], and homogeneous strain tensor η_H . The total energy of the effective Hamiltonian has two main terms

$$E_{\text{tot}} = E_{\text{dipole}}(\{\mathbf{u}_i\}, \{\mathbf{v}_i\}, \eta_H) + E_{\text{AFD}}(\{\mathbf{u}_i\}, \{\mathbf{v}_i\}, \{\boldsymbol{\omega}_i\}, \eta_H), \quad (1)$$

where E_{dipole} is the energy of local soft modes, strains and their coupling, including five main terms [37], namely, the quartic soft mode self-energy, the quadratic soft mode long-range dipolar energy, the quadratic soft mode short-range interaction energy (up to the third nearest neighbor), the elastic energy (including both homogeneous and inhomogeneous contributions), and the interaction between soft mode and strain (quadratic in soft mode and linear in strain); the E_{AFD} is the energy of AFD motions and their coupling with strains and soft modes, including the quartic AFD onsite energy, the quadratic and quartic AFD short-range interaction energy (up to the first neighbor), the interaction between AFD and strain (quadratic in AFD and linear in strain), and the biquadratic and trilinear interaction between soft mode and AFD motion. The interaction coefficients are greatly simplified due to the symmetry. The complete analytical form of the effective Hamiltonian is proposed in Ref. [36]. An additional term $-Z^* \sum_i \mathbf{u}_i \cdot \mathbf{E}$ is added in E_{tot} to consider the effect of external electric field [38], where the summation of i runs over all the unit cells in the simulated supercell, Z^* is the Born effective charge of the soft mode, and \mathbf{E} is the external electric field. Note that considering the electric field in atomic schemes (such as the effective Hamiltonian approach employed here) are typically overestimated by 1 to 2 orders of magnitudes due to the fact of Landauer paradox [39–41], the electric field is rescaled linearly by $\tilde{\mathbf{E}} = c\mathbf{E}$, where \mathbf{E} and $\tilde{\mathbf{E}}$ are the original and rescaled field, and c is 0.2 here which gives perfectly consistency with measurement for the calculation of ECE in Pb(Sc_{0.5}Ta_{0.5})O₃ [41]. The quantities related to the rescaled electric field are marked with a tilde throughout this manuscript.

The perovskite structures are typically simulated by $12 \times 12 \times 12$ supercells (corresponding to 8640 atoms) or large

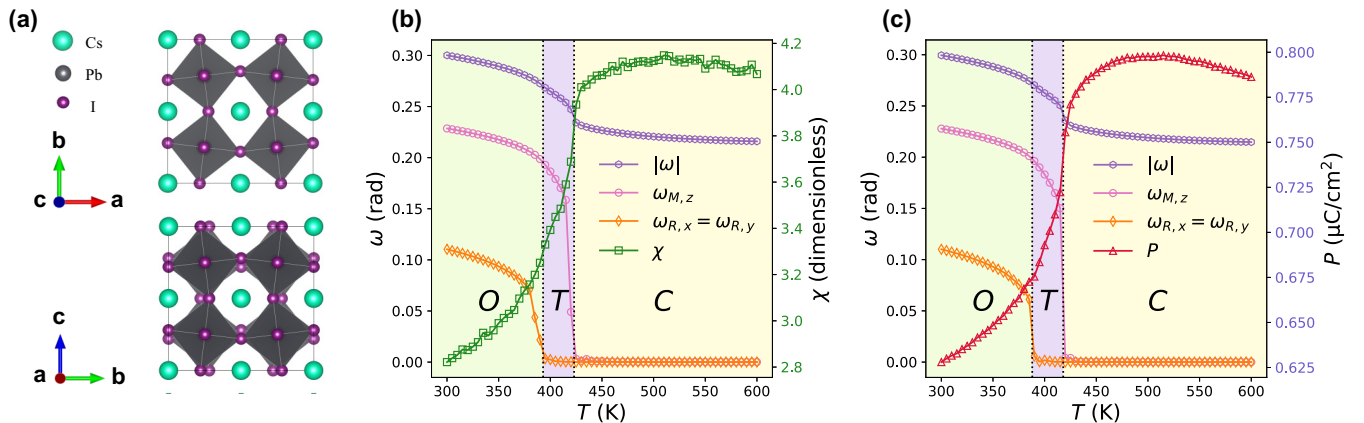


FIG. 2. Structures and phase diagram of CsPbI₃. (a) Schematics of AFD motions. The top and bottom panels represent the AFD pattern of $\omega_{M,z}$ and $\omega_{R,x}$, respectively. (b) AFD vectors $\omega_{M,z}$, $\omega_{R,x}$ ($\omega_{R,y}$) and $|\omega|$, and electric susceptibility χ as a function of temperature at zero field. (c) AFD vectors $\omega_{M,z}$, $\omega_{R,x}$ ($\omega_{R,y}$), and $|\omega|$, and polarization P as a function of temperature under electric field of 0.43 MV/cm along the pseudocubic [110] direction.

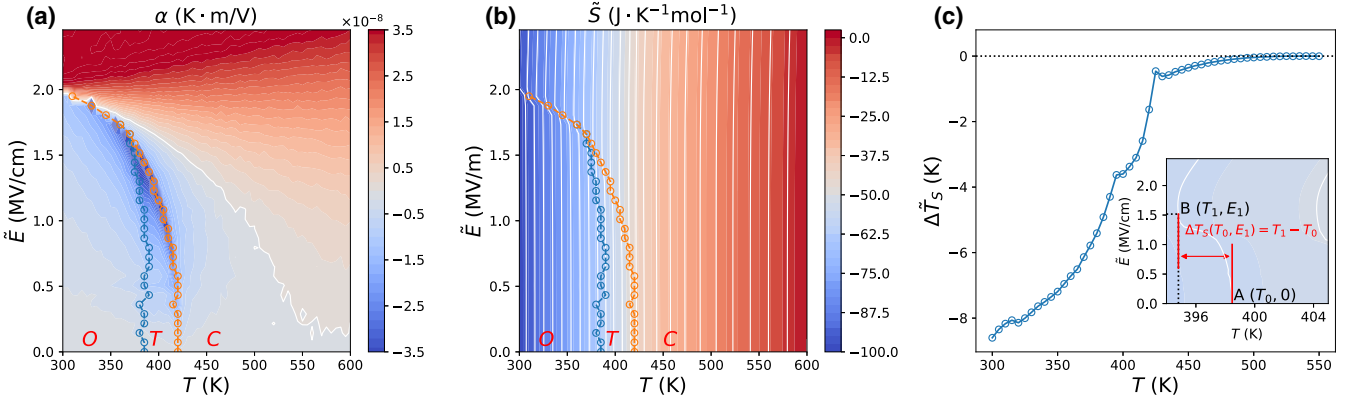


FIG. 3. Inverse ECE in CsPbI₃ for a wide range of temperature. (a) Electrocaloric coefficient α as functions of electric field \tilde{E} and temperature T . The white solid line denotes the $\alpha = 0$ isoline. (b) Relative entropy \tilde{S} as functions of electric field \tilde{E} and temperature T . (c) Maximal negative adiabatic temperature change induced by applying electric field near the phase boundary of brown line shown in (a) and (b) as a function of temperature. (Inset) Sketch of the numeric scheme used for calculating the adiabatic temperature change. The blue and orange circles in (a) and (b) denote the phase boundaries between the O, T, and C phases.

$32 \times 32 \times 32$ supercells (corresponding to 163 840 atoms) with Monte Carlo (MC) simulations. The following quantities are computed: (i) The AFD at R point characterizing antiphase tilting, defined as $\omega_R = \frac{1}{N} \sum_i \omega_i (-1)^{n_x(i)+n_y(i)+n_z(i)}$, where the summation of i runs over all of the N five-atom perovskite unit cells in the simulated supercell, ω_i is the AFD vector of unit cell located at $a_0(n_x(i)\hat{x} + n_y(i)\hat{y} + n_z(i)\hat{z})$, a_0 is the lattice constant of the five-atom perovskite unit cell, and $\hat{x}, \hat{y}, \hat{z}$ are the unit vectors along the pseudocubic [100], [010], and [001] directions, respectively; (ii) the AFD at M point characterizing the in-phase tilting, defined as $\omega_M = \frac{1}{N} \sum_i \omega_i (-1)^{n_x(i)+n_y(i)}$; (iii) the average absolute value of local AFD vectors $|\omega| = \frac{1}{N} \sum_i |\omega_i|$; (iv) the average soft mode motion $\mathbf{u} = \frac{1}{N} \sum_i \mathbf{u}_i$; (v) the polarization $\mathbf{P} = \frac{1}{\Omega} Z^* \mathbf{u}$, where Ω is the volume of the simulated supercell; and (vi) the antipolar soft mode motion at X point $\mathbf{u}_X = \frac{1}{N} \sum_i \mathbf{u}_i (-1)^{n_x(i)}$.

The dielectric susceptibility tensor χ shown in Fig. 2(b) and the EC coefficient α shown in Fig. 3(a) are computed from the MC simulations with the cumulant formula [39,42,43].

The isothermal entropy change is calculated using the numerical method developed in Ref. [41] as

$$\Delta S = \frac{1}{T} \left(\Delta H + \int \Omega \mathbf{P} \cdot d\mathbf{E} \right), \quad (2)$$

where H is the enthalpy calculated by

$$H = E_{\text{tot}} + \frac{21}{2} N k_B T + p \Omega - \Omega \mathbf{E} \cdot \mathbf{P}, \quad (3)$$

where N is the number of unit cells in the supercell, k_B is the Boltzmann constant, T is the temperature, E_{tot} is the energy of effective Hamiltonian provided in Eq. (1), and p is the external pressure ($p = 0$ in this work), \mathbf{E} is the external electric field, and \mathbf{P} is the polarization of the supercell. The entropy change as a function of temperature with absent of electric field is computed by

$$\Delta S|_{E=0} = \int \frac{1}{T} dH = \Delta \left(\frac{H}{T} \right) + \int \frac{H}{T^2} dT. \quad (4)$$

The relative entropy diagram $\tilde{S}(T, \tilde{E})$ is thus determined from Eqs. (2) and (4), as shown in Fig. 3(b). The adiabatic tem-

perature change $\Delta \tilde{T}_S$ is calculated from the relative entropy diagram. More precisely, the inset of Fig. 3(c) shows the sketch for such scheme, which is taken from the zoom in view of Fig. 3(b). To evaluate the temperature change induced by applying electric field adiabatically from a specified temperature T_0 (point A in the sketch), the isentropic line passing such point in the (T, \tilde{E}) diagram is first identified (see the white solid line in the sketch). Then, for each electric field \tilde{E}_1 , the point on the isentropic line with such electric field is identified (see point B in the sketch), and the temperature of such point is denoted as T_1 . Then, the adiabatic temperature change induced by applying electric field adiabatically is calculated from

$$\Delta \tilde{T}_S(T_0, \tilde{E}_1) = T_1 - T_0. \quad (5)$$

Taken the present case of the inset of Fig. 3(c) as an example, in which $T_0 = 398.5$ K, $E_1 = 1.52$ MV/cm, and $T_1 = 394.8$ K. Then, the adiabatic temperature change is $\Delta \tilde{T}_S(398.5\text{K}, 1.52 \text{ MV/cm}) = -3.7$ K.

B. Hybrid Monte Carlo simulation

Hybrid Monte Carlo (HMC) algorithm [44–46] is implemented for large-scale simulations. In each Monte Carlo sweep (MCS) of the HMC simulations, a new trial configuration of $\{\mathbf{u}_i\}$, $\{\mathbf{v}_i\}$, and $\{\omega_i\}$ is generated by performing microcanonical molecular dynamics (MD) simulation for a short period with random initial momenta. Benefitted from the energy conservation nature of the microcanonical MD simulation in the HMC sweeps, the acceptance ratio of the hybrid Monte Carlo sampling could be rather high. Practically in this work, each trial configuration is generated by performing 40 MD steps with integration step of 1 fs, and the acceptance ratio is typically over 98%. Note that in Monte Carlo simulations with classic METROPOLIS algorithm [47], such acceptance ratio is typically between 20% and 40%, indicating that about 60% to 80% of the computational effort may be wasted [37,46]. The homogeneous strain η_H is practically updated using the standard METROPOLIS algorithm as in Ref. [37].

Technically, the long-range dipole energy

$$E_{\text{dpl}} = \sum_{ij\alpha\beta} Q_{\alpha\beta}(\mathbf{r}_i - \mathbf{r}_j) u_{\alpha}(\mathbf{r}_i) u_{\beta}(\mathbf{r}_j) \quad (6)$$

and forces associated with it are computed in the reciprocal space with the help of fast Fourier transformation algorithm, as in Refs. [46,48,49]. Such treatment reduces the overall computation complexity of one MCS from $O(N^2)$ in standard METROPOLIS algorithm to $O(N \ln N)$. Moreover, in the MD simulations, the degrees of freedom of all unit cells are updated simultaneously, in contrast with METROPOLIS MC simulation, in which the degrees of freedom are updated in sequence. Such simultaneous update makes it easy to run the HMC simulations *in parallel*, especially on shared memory architectures [46]. The reduced complexity and ability to run in parallel makes it possible to perform simulations on large supercells efficiently.

Moreover, computational efficiency tests were performed for the $E_{\text{elas},I}$ in Ref. [37] and the following terms (in notations of Refs. [36,37]):

$$E_{\text{mode-strain}} = \frac{1}{2} \sum_i \sum_{l\alpha\beta} B_{l\alpha\beta} \eta_{l,l}(\mathbf{r}_i) u_{\alpha}(\mathbf{r}_i) u_{\beta}(\mathbf{r}_i), \quad (7)$$

$$E_{\text{AFD-strain}} = \frac{1}{2} \sum_i \sum_{l\alpha\beta} C_{l\alpha\beta} \eta_{l,l}(\mathbf{r}_i) \omega_{\alpha}(\mathbf{r}_i) \omega_{\beta}(\mathbf{r}_i), \quad (8)$$

$$E_{\text{mode-AFD},1} = \sum_{ij} \sum_{\alpha\beta} D_{ij\alpha\beta} u_{\alpha}(\mathbf{r}_j) \omega_{\alpha}(\mathbf{r}_i) \omega_{\beta}(\mathbf{r}_i), \quad (9)$$

$$E_{\text{mode-AFD},2} = \sum_{ij} \sum_{\alpha\beta\gamma\delta} E_{\alpha\beta\gamma\delta} \omega_{\alpha}(\mathbf{r}_i) \omega_{\beta}(\mathbf{r}_i) u_{\gamma}(\mathbf{r}_j) u_{\delta}(\mathbf{r}_j), \quad (10)$$

where the summation of i runs over all the unit cells in the supercell, the summation of j runs over several neighbor cells around i , $\{\eta_l\}$ is the inhomogeneous strain which is computed from $\{\mathbf{v}_i\}$ [37], $\alpha, \beta, \gamma, \delta$ are cartesian directions, and $l = 1, 2, \dots, 6$ is the Voigt notation index. Such tests show that it is more efficient to compute these terms (as well as their associated forces) in the reciprocal space, although they have in principle complexity of $O(N)$ calculating in the real space.

C. Phenomenological model

To understand the ECE in perovskites, the Landau-like model is constructed with four types of nonvanishing order parameters and the homogeneous strain. The four order parameters are (i) AFD motion at M point $\omega_{M,z} = \omega$, (ii) AFD motion at R point $\omega_{R,x} = \omega_{R,y} = \theta$, (iii) antipolar soft mode motion at X point $u_{X,x} = u_{X,y} = s$, and (iv) polar soft mode motion at Γ point $u_x = u_y = u$ (which is fully driven by external electric field). According to the symmetry, the components of the homogeneous strain are $\eta_1 = \eta_2 = \eta_a$, $\eta_3 = \eta_b$, $\eta_4 = \eta_c$, and $\eta_5 = \eta_6 = \eta_d$. Therefore, using ω, θ, s, u and $\eta_a, \eta_b, \eta_c, \eta_d$ as order parameters, the Landau-like model could be written as

$$\begin{aligned} H_{\text{model}} = & a_u u^2 + b_u u^4 + a_s s^2 + b_s s^4 \\ & + a_{\omega} \omega^2 + b_{\omega} \omega^4 + a_{\theta} \theta^2 + b_{\theta} \theta^4 \\ & + c_1 u^2 s^2 + c_2 \omega^2 \theta^2 + d s \omega \theta \end{aligned}$$

$$\begin{aligned} & + f_1 \theta^2 (u^2 + s^2) + f_2 \omega^2 (u^2 + s^2) \\ & + E_{\text{elas}} + E_{\text{polar-elas}} + E_{\text{tilt-elas}} - 2Z^* E u, \quad (11) \end{aligned}$$

where $\tilde{E}_x = \tilde{E}_y = E$ is the components of external electric field, and E_{elas} is the energy associated with the homogeneous strain whose details can be found in Ref. [37], $E_{\text{polar-elas}}$ and $E_{\text{tilt-elas}}$ have following forms:

$$\begin{aligned} E_{\text{polar-elas}} = & B_{1xx} \eta_a (u^2 + s^2) + B_{1yy} (\eta_a + \eta_b) (u^2 + s^2) \\ & + B_{4yz} \eta_c (u^2 + s^2) \quad (12) \end{aligned}$$

and

$$\begin{aligned} E_{\text{tilt-elas}} = & \frac{1}{2} C_{1xx} (2\eta_a \theta^2 + \eta_b \omega^2) \\ & + C_{1yy} (\eta_a \theta^2 + \eta_a \omega^2 + \eta_b \theta^2) + C_{4yz} \eta_c \theta^2. \quad (13) \end{aligned}$$

Note that the parameters in this model of Eq. (11) can be directly derived from the parameters used in our effective Hamiltonian which has been confirmed by first principles calculations [36]. For example, $b_u = b_s = 4\alpha + \gamma$ and $f_2 = 2E_{\text{xyyy}}$, where α, γ , and E_{xyyy} are the parameters of effective Hamiltonian calculations [36]. Table I shows the values of the parameters in the model of Eq. (11).

To further understand the ECE from the entropy concept quantitatively, the isothermal entropy change induced by applying electric field is calculated within the model of Eq. (11) using Eq. (2). The isothermal entropy change can be split into four parts

$$\Delta S = \Delta S_{\text{polar}} + \Delta S_{\text{tilt}} + \Delta S_{\text{coup}} + \Delta S_{\text{field}}, \quad (14)$$

where ΔS_{polar} is the entropy change only comes from the soft mode, antipolar motion, strain, and their coupling

$$\begin{aligned} \Delta S_{\text{polar}} = & \frac{1}{T} [a_u \Delta(u^2) + b_u \Delta(u^4) \\ & + a_s \Delta(s^2) + b_s \Delta(s^4) + c_1 \Delta(u^2 s^2) \\ & + E_{\text{elas}, H} + E_{\text{polar-elas}}], \quad (15) \end{aligned}$$

ΔS_{tilt} is the contribution only from AFD motion and its coupling with strain

$$\begin{aligned} \Delta S_{\text{tilt}} = & \frac{1}{T} [a_{\omega} \Delta(\omega^2) + b_{\omega} \Delta(\omega^4) \\ & + a_{\theta} \Delta(\theta^2) + b_{\theta} \Delta(\theta^4) + c_2 \Delta(\theta^2 \omega^2) \\ & + E_{\text{tilt-elas}}], \quad (16) \end{aligned}$$

ΔS_{coup} is the entropy change comes from the coupling terms between soft mode and AFD

$$\begin{aligned} \Delta S_{\text{coup}} = & \frac{1}{T} [d \Delta(s \theta \omega) + f_1 \Delta(\theta^2 (u^2 + s^2)) \\ & + f_2 \Delta(\omega^2 (u^2 + s^2))], \quad (17) \end{aligned}$$

ΔS_{field} is the contribution directly related to the electric field

$$\Delta S_{\text{field}} = \frac{2Z^*}{T} \left[\int u dE - \Delta(Eu) \right]. \quad (18)$$

The notation $\Delta(g)$ means the change of value g in the isothermal process. Particularly, the entropy change associated with

TABLE I. Parameters for Landau-like model. Values are given in atomic units.

	a_u	b_u	a_s	b_s	a_ω	b_ω	a_θ	b_θ
CsPbI ₃	-0.000486	0.00270	-0.000530	0.00270	-0.1017	0.9914	-0.1828	4.102
PbSc _{0.5} Ta _{0.5} O ₃	-0.0198	0.0519	-0.00369	0.0519	-0.1981	3.777	-0.4538	13.375
	c_1	c_2	d	f_1	f_2	c_1/a_u	f_1/a_u	f_2/a_u
CsPbI ₃	0.0162	4.216	-0.2574	0.07393	0.07118	-33.341	-152.155	-146.496
PbSc _{0.5} Ta _{0.5} O ₃	0.3112	10.482	0.1620	0.8357	0.7556	-15.714	-42.196	-38.153

antipolar motion $\Delta S_{\text{antipolar}}$, which is also a part of ΔS_{polar} , is given by

$$\Delta S_{\text{antipolar}} = \frac{1}{T} [a_s \Delta(s^2) + b_s \Delta(s^4)]. \quad (19)$$

III. RESULTS

A. Structures at finite temperature

We first investigated structures and EC properties of halide perovskite structure of CsPbI₃ at finite temperature. Figure 2(b) shows average AFD motions of in-phase tilting at M point ($\omega_{M,z}$) and antiphase tilting at R point ($\omega_{R,x}$) in supercell as a function of temperature [see Fig. 2(a) about schematics of such motions]. At high temperature larger than 420 K, the statistical averages of ω_M and ω_R are zero, characterizing a cubic $Pm\bar{3}m$ phase (C phase). As the temperature decreases to 420 K, $\omega_{M,z}$ shows a nonzero average value while ω_R is still zero, characterizing a tetragonal $P4/mbm$ phase (T phase) with iodine octahedra tilting pattern $a^0 a^0 c^+$ (Glazer's notation [50]). As for the temperature smaller than 390 K, both $\omega_{R,x}$ and $\omega_{M,z}$ have nonzero values. The $\omega_{R,x}$ and $\omega_{R,y}$ always have almost identical values below 390 K, characterizing an orthorhombic $Pnma$ phase with tilting pattern $a^- a^- c^+$ (O phase). The phase diagram is consistent with experimental measurement [51] and previous calculations [36]. Note that Figs. 2(b) and 2(c) also show the average absolute value of AFD $|\omega|$, which possesses a finite value at all investigated temperatures, even for the C phase where both ω_M and ω_R vanish, indicating the existence of the disordered local AFD in the C phase.

Figure 2(c) shows AFD vectors $\omega_{M,z}$ and $\omega_{R,x}$ as a function of temperature under electric field of $\vec{E} = 0.43$ MV/cm. This phase diagram is very similar to that in the absence of the electric field. The phase transition from the C to T phase occurs at the temperature of 415 K, and the transition from the T to O phase occurs at 385 K. Both transition temperatures are slightly smaller than that at zero electric field by 5 K. Interestingly, the polarization shown in Fig. 2(c) driven by external electric field *decreases* with the decreasing of temperature. This is different from prototypical ferroelectrics where the polarization increases with the decrease of temperature and becomes large at lower temperature. This unusual phenomenon of polarization driven by electric field with respect to temperature implies the abnormal temperature response under electric field. Note that due to the soft mode motion under finite electric field, the symmetry group of the three phases under the application of electric field are no longer *exactly* $Pm\bar{3}m$, $P4/mbm$, and $Pnma$, but adopt lower symmetry. However, the notations of the C, T, and O phases are

still used, since the AFD motions at small fields are similar to that in the absence of electric field (see Fig. 2), and the soft mode motion is rather small. As the electric field increase above 2.0 MV/cm, no phase transition is observed, and the AFD vectors ω_R , ω_M remain zero in the whole investigated temperature range.

B. Inverse ECE in broad range of temperature

Figure 3(a) shows the calculated EC coefficient α as functions of temperature T and the applied electric field \vec{E} along the pseudocubic [110] direction, in which the white solid line is the isoline of a zero EC coefficient α . The EC coefficient is positive above this isoline (red color), indicating normal ECE, which generally exists in normal paraelectric materials [52]. The EC coefficient is negative in a large region below such isoline (blue color). Interestingly, this inverse ECE exists in all the nonpolar phases at a large range of temperature from 300 K to ≈ 550 K, very different from that in the previous studies, where the inverse ECE is typically found in antiferroelectrics phase in a relatively narrow range of temperature [28,29]. Figure 3(b) shows the calculated relative entropy diagram $\tilde{S}(T, \vec{E})$, where the isentropic lines are depicted by the white solid lines. The adiabatic system evolves in one isentropic line in a reversible process. On tracing the isentropic lines in the direction of increasing field [i.e., from the bottom to the top in Fig. 3(b)], the left (respectively, right) bending of isentropic lines imply inverse (respectively, normal) ECE. Figure 3(c) shows the maximal negative adiabatic temperature change ($\Delta\tilde{T}_S$) as a function of starting temperature, which is the temperature change ($\Delta\tilde{T}_S$) when tracing the isentropic lines in Fig. 3(b) under electric field. The magnitude of negative adiabatic temperature change is large (up to -8.6 K) at low temperature about 300 K, and decreases with the increase of temperature. The negative temperature change is larger than 2 K over a broad range of temperature from 300 to 415 K.

From Eq. (11), as the external electric field only couples with soft mode motion directly, the enthalpy change induced by change of soft mode under small electric field (where inverse ECE is observed) has the form

$$dH_{\text{model}} = \{2a_u u + 2(c_1 s^2 + f_1 \theta^2 + f_2 \omega^2)u + 4b_u u^3 + 2[B_{1xx}\eta_a + B_{1yy}(\eta_a + \eta_b) + B_{4yz}\eta_c]u - 2Z^*E\}du, \quad (20)$$

where the last term is directly induced by the electric field and is constant under a given magnitude of electric field, and the third term could be neglected for small u . As shown in Table I, the parameter a_u for the first term is negative, indicating the

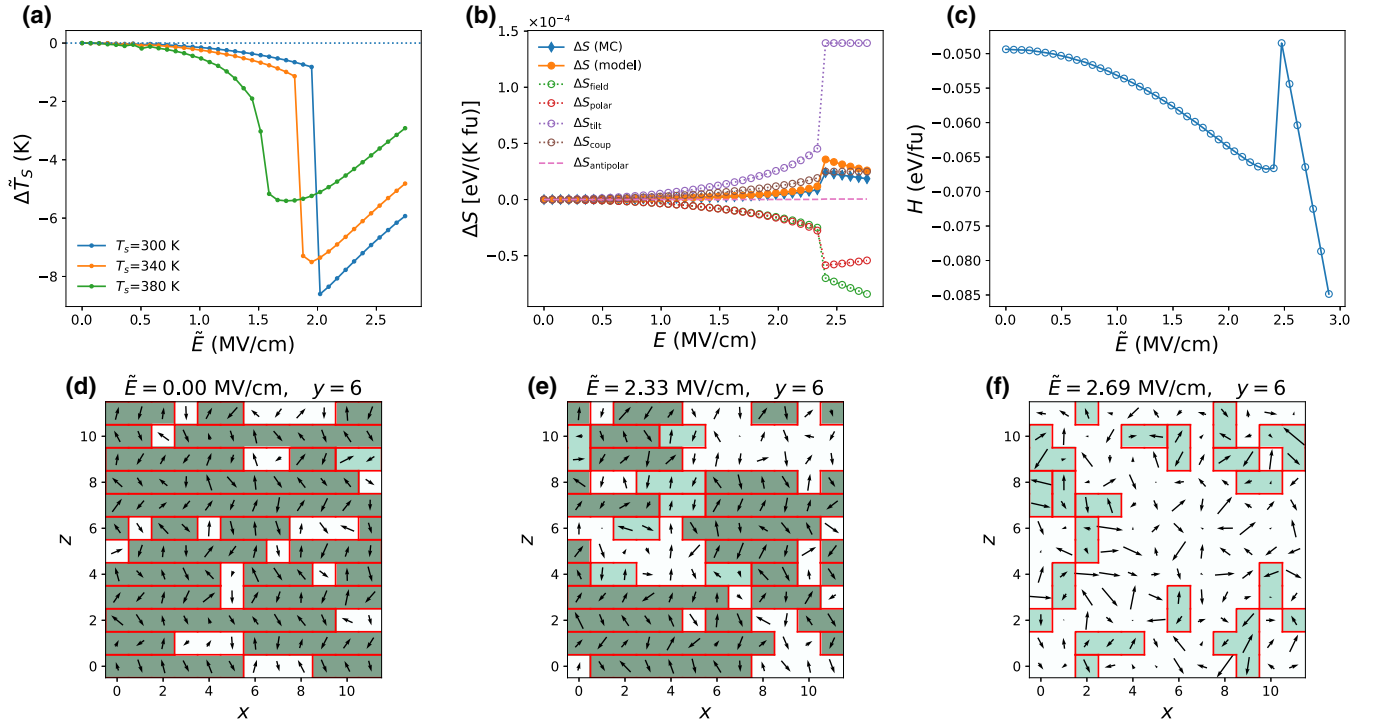


FIG. 4. Inverse ECE in O phase. (a) Adiabatic temperature changes induced by applying electric field starting from the temperature of 300, 340, and 380 K. (b) Isothermal entropy changes per formal unit (fu) from the MC simulation [ΔS (MC)], the model of Eq. (14) [ΔS (model)] and its contribution from each term, as a function of electric field at 300 K. (c) Total enthalpy H as a function of applied electric field along pseudocubic [110] direction at 300 K. [(d), (e), and (f)] Local AFD snapshots at 300 K under electric field of 0.00, 2.33, and 2.69 MV/cm, respectively. Each arrow represents a local AFD vector in a unit cell, and the red lines delimit the AFD clusters $AFD_{R,cl}$. Light green color denotes AFD vectors belonging to $AFD_{R,cl}$, dark green background represents percolated $AFD_{R,cl}$.

instability of soft mode distortion. For the second term, the large positive c_1 , f_1 and f_2 imply the strong coupling between AFD (θ and ω), antipolar (s) and soft mode (u) motion, and the antipolar and AFD motion tend to restrain the soft mode distortion. The fourth term typically has small magnitude comparing with the second one. The values of the same parameters for $PbSc_{0.5}Ta_{0.5}O_3$ (PST) [41] which possesses positive ECE are also listed in Table I for comparison. One can see the f_1/a_u , f_2/a_u , c_1/a_u for PST have much smaller magnitudes than those in $CsPbI_3$, indicating the coupling between soft mode motions and AFD as well as antipolar motion are *not* strong enough to suppress the soft mode motions in PST, which does not possess inverse ECE.

The strong competition between soft mode motion and AFD motion ($f_1\theta^2u^2$ and $f_2\omega^2u^2$) can be confirmed by AFD and polarization in Fig. 2(c). At the small electric field 0.43 MV/cm, the magnitude of $\omega_{M,z}$ and $\omega_{R,x}$ increase with the decreasing of temperature in the T and O phases, while the polarization decreases with the decreasing of temperature from about 500 K. Therefore the derivative of polarization P (or the soft mode u) with respect to temperature below $\simeq 500$ K at small constant field is positive

$$\left(\frac{\partial P}{\partial T}\right)_E > 0. \quad (21)$$

This contrasts to the fact in prototypical ferroelectrics where the polarization increases with the decrease of temperature. As suggested by Maxwell relations, the EC coefficient could

be written as [2,39]

$$\alpha = -\frac{T}{C_E} \left(\frac{\partial P}{\partial T}\right)_E, \quad (22)$$

where C_E is the heat capacity at constant electric field and is positive. It is thus clear that the positive value of $(\frac{\partial P}{\partial T})_E$ would result in negative value of α (that is inverse ECE). Such analysis implies that the inverse ECE below $\simeq 500$ K originates from the strong coupling between AFD and soft mode.

C. Inverse ECE in the O phase

The structure of $CsPbI_3$ is the O phase below the temperature 390 K without applying electric field. The O phase possesses inverse ECE [blue color below the white line in Fig. 3(a) at small electric field]. At the electric field above 2.0 MV/cm, the O phase transforms into the C phase, and the ECE becomes normal. To further investigate the inverse ECE, Fig. 4(a) shows the adiabatic temperature change $\Delta\tilde{T}_S$ due to the application of electric field, from the initial temperatures of 300, 340, and 380 K. For the adiabatic process starting from 300 K, the temperature decreases slightly as the electric field increases from 0 MV/cm, which is consistent with the negative EC coefficient [see Fig. 3(a)]. The temperature drop is about -0.82 K at 1.95 MV/cm. As the electric field further increases and passes through the phase boundary between the O and C phases, the temperature change drops drastically to -8.6 K. The further increasing of electric field larger than

2.0 MV/cm results in the increase of the temperature change (normal ECE). The adiabatic process starting from 340 K behaves similarly to that starting from 300 K, possessing a temperature jump at 1.8 MV/cm with an extreme value of -7.5 K. For the starting temperature of 380 K, the temperature change drop occurs at the phase boundary line between the O and T phases at lower electric field about 1.5 MV/cm, and exhibits a broader valley at the vicinity of phase boundaries.

To figure out the entropy change in the phenomena of inverse ECE in the O phase, Fig. 4(b) shows the isothermal entropy change computed from the MC simulations by Eq. (2) [ΔS (MC)], the model of Eq. (14) [ΔS (model)], and the different terms in Eq. (14), as a function of electric field in an isothermal process at 300 K. The ΔS (model) curve is consistent with the ΔS (MC) curve very well, indicating the validity of the model of Eqs. (11) and (14). The $\Delta S_{\text{antipolar}}$ [Eq. (19)] is close to zero. The ΔS_{field} and ΔS_{polar} curves show negative values in the whole investigated field range, while the ΔS_{tilt} and ΔS_{coup} display positive values. The positive total entropy change mainly comes from the large ΔS_{tilt} . Furthermore, the positive ΔS_{coup} is the entropy change from coupling between AFD and polar or antipolar motion. Therefore the positive entropy change ΔS (model) and the resulting inverse ECE come from the AFD related entropy change. The conclusion that the inverse ECE is induced by the AFD related entropy change contrasts to the literature [2,28] in which antipolar entropy change is proposed to leading to the inverse ECE. Note that the AFD (ω and θ) does *not* interplay with electric field directly (see the full analytical form of the effective Hamiltonian [36]) but couples with u by $\omega^2 u^2$ and $\theta^2 u^2$, which leads to the AFD related entropy change due to u (or polarization) responsible for the electric field indirectly.

On the other hand, near 2.4 MV/cm, the ΔS_{tilt} and ΔS_{coup} terms exhibit a sudden positive jump, leading to a jump of total entropy. In Fig. 4(c), the enthalpy also exhibits a sudden jump near 2.4 MV/cm. Such jumps of entropy and enthalpy are caused by the phase transition from the O to C phase driven by the external electric field, which is endothermic in nature. Further more, such phase transition takes place from an ordered state (with nonvanishing statistical average of $\omega_{M,z}$ and $\omega_{R,x}$ in the O phase) to a disordered state (with vanishing order of AFD pattern as well as statistical average of $\omega_{M,z}$ and $\omega_{R,x}$ in the C phase). The disordering of AFD motion contributes greatly to the overall entropy, resulting in the large inverse ECE near the transition [Fig. 4(a)]. This endothermic phase transition induced inverse ECE also occurs in PbZrO_3 [29].

In order to gain a microscopic understanding of the AFD entropy change, the *local clusters* $\text{AFD}_{R,cl}$ (or $\text{AFD}_{M,cl}$) are defined to describe the local ordering of the AFD pattern. At finite temperature under electric field, the AFDs are not fully ordered, but partially ordered. The $\text{AFD}_{R,cl}$ (respectively, $\text{AFD}_{M,cl}$) is defined as the local clusters in which the AFD vector in each unit cell $\omega_R(i) = (-1)^{n_x(i)+n_y(i)+n_z(i)} \omega_i$ [respectively, $\omega_M(i) = (-1)^{n_x(i)+n_y(i)}$] are nearly parallel to each other. The *local clusters* $\text{AFD}_{K,cl}$ (where K corresponds to R or M here) are practically identified by comparing directions of $\omega_K(i)$ with their nearest neighbors [53], two neighbor AFD vectors are considered to belong to the same cluster if the cosine of the angle between them is larger than 0.85. The *local*

clusters $\text{AFD}_{K,cl}$ can be described by size $\langle s \rangle$ (which is the number of units in the cluster) and the average magnitude of the AFD vector in the cluster $\omega_{K,\alpha}^{\text{clus}}$ defined by

$$\omega_{K,\alpha}^{\text{clus}} = \frac{1}{N_t} \sum_j |\omega_{R,\alpha}(j)|, \quad (23)$$

where α is the cartesian direction index, j sums over all the unit cells that belongs to a local AFD cluster with size larger than 1, and N_t is the number of such unit cells in the simulated supercell. Note that the cluster can propagate from one side of the supercell to its opposite side, which is the so-called *AFD percolation*, the cluster of *AFD percolation* has infinite size under periodic boundary conditions.

As shown in Figs. 4(d)–4(f), the size $\langle s \rangle$ of the *AFD cluster* decreases when the electric field increase. Almost all unit cells belong to the clusters of percolation in the absence of field, some AFD vector do not belong to the AFD cluster and percolation at electric field of 2.33 MV/cm, and there is no percolation and most AFD vector do not belong to clusters at the electric field of 2.69 MV/cm. The ordered AFD vectors in the absence of field become disordered at high electric field, and the AFD entropy increases with the increase of electric field.

D. Inverse ECE in the T phase

The ECE in the T phase is then investigated. As shown in Fig. 3(a), the T phase possesses inverse ECE at low electric field. The EC coefficient exhibits large negative value at the phases boundary of the O, T, and C phases near the temperature of 390 K under electric field of 1.4 MV/cm. This large negative EC coefficient [dark blue color in Fig. 3(a)] exists in a wide range of electric field from 1.3 to 2.0 MV/cm. Figure 5(a) shows the adiabatic temperature change as a function of electric field starting from the temperatures of 400, 410, and 420 K, where the structure of CsPbI_3 is the T phase at zero electric field. At low field, the larger the starting temperature is, the faster adiabatic temperature change ($\Delta \tilde{T}_S$) drops, and the smaller the maximal negative adiabatic temperature change is. For a starting temperature of 400, 410, and 420 K, the maximal negative adiabatic temperature changes are -3.6 K at about 1.7 MV/cm, -3.1 K at about 1.6 MV/cm, and -1.6 K at about 1.5 MV/cm, respectively. Note that the maximal adiabatic temperature change terrace $\Delta \tilde{T}$ presents at larger range of temperature than that of the O phase [see Fig. 4(a)], which is consistent with Fig. 3(a).

To understand the unexpected inverse ECE in the T phase, the entropy change is analyzed with the model proposed in Eqs. (11) and (14). In the T phase, the antipolar motion s is zero and the antipolar entropy change $\Delta S_{\text{antipolar}}$ is zero. Note that the AFD at R point (θ) is in principle zero in the whole supercell of the T phase. However, considering the AFD may be partially ordered and form local AFD cluster [54], here the θ is numerically defined as the average value of ω_R in $\text{AFD}_{R,cl}$ clusters, i.e., $\omega_{R,x}^{\text{clus}}$. Figure 5(c) shows the snapshot taken from MC simulation at 410 K at the absent of electric field, confirming the existence of $\text{AFD}_{R,cl}$ clusters in the macroscopic T phase. It is numerically found such treatment of θ is essential for our model to reproduce the entropy change from MC calculations correctly. Figure 5(b) shows the isothermal entropy change computed from MC

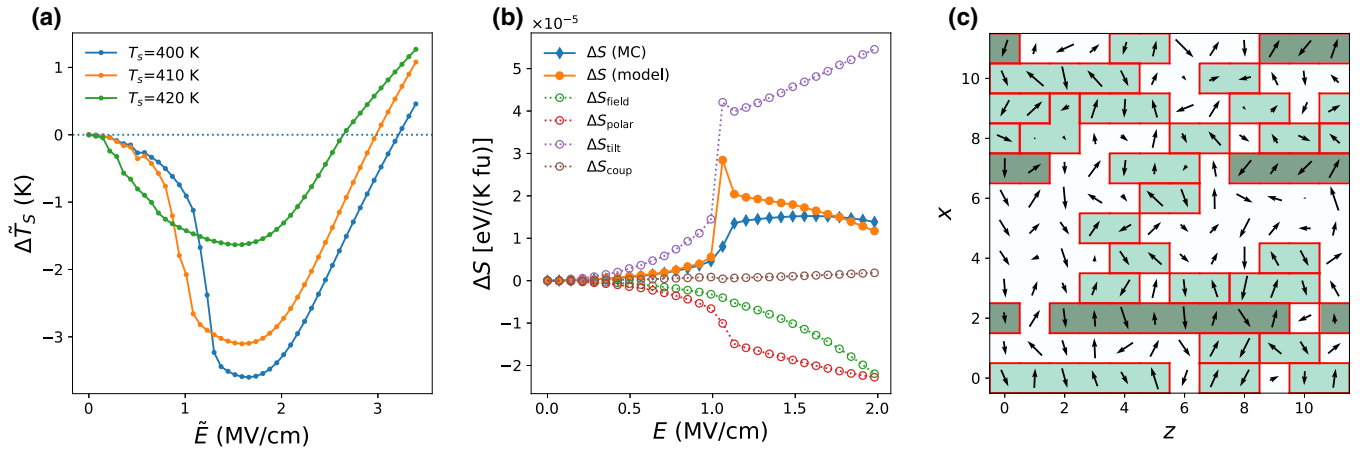


FIG. 5. Inverse ECE in T phase. (a) Adiabatic temperature changes induced by applying electric field starting from 400, 410, and 420 K in the T phase. (b) Isothermal entropy change induced by applying electric field computed directly from MC results [ΔS (MC)], the simplified model [ΔS (model), Eq. (14)], and the contribution from each term (defined in text), as a function of electric field at 400 K. (c) Schematics of AFD cluster $AFD_{R,cl}$ taken from MC simulation at 410 K in the absence of field. The arrows denote the local AFD vectors, and the red lines delimit the AFD clusters $AFD_{R,cl}$. Light green color denotes AFD vectors belonging to $AFD_{R,cl}$, dark green background represents percolated $AFD_{R,cl}$.

simulation [ΔS (MC)], the model proposed in Eq. (14) [ΔS (model)] and its contribution from each term, as a function of electric field at 400 K. The ΔS (model) is consistent very well with the ΔS (MC) at low field and also close to each other at high field. Similar to the case of the O phase, the ΔS_{field} and ΔS_{polar} terms possess large negative values. The positive contribution mainly comes from ΔS_{tilt} . It is thus clear that the fundamental origin of inverse ECE in the T phase is also the tilting entropy. Note that the contribution from ΔS_{coup} is rather small in the T phase, in contrast with that in the O phase, where the ΔS_{coup} has significantly positive value [see Fig. 4(b)]. It is numerically found that such difference stems from the trilinear coupling term $d\Delta(s\theta\omega)$ of Eq. (17) in the O phase. In fact, the trilinear term is the main contribution to ΔS_{coup} in the O phase. However, such term vanishes in the T phase, since the antipolar motion s is zero in this phase, leading to the small total value of ΔS_{coup} .

E. Electrocaloric response in the C phase

The C phase of CsPbI_3 also presents the inverse ECE. As shown in Fig. 6(a), the adiabatic temperature change starting from 450 and 500 K can be negative at low electric field. The negative adiabatic temperature starting from 450 K reaches the maximum of -0.36 K at the electric field of 1.37 MV/cm. This maximum of the inverse ECE occurs at the critical electric field where $\alpha = 0$ shown in Fig. 3(a). The inverse ECE become weaker when the starting temperature increases, characterized by the decreasing absolute values of temperature change under electric field. The inverse ECE vanishes completely at the starting temperature of 550 K, where the adiabatic temperature change is positive for all investigated magnitudes of electric field, consistent with the fact that the α is almost always positive at temperature larger than 550 K. The ECE becoming normal at the temperature larger than 550 K is also consistent with the fact that $(\frac{\partial P}{\partial T})_E$ is negative at low electric field [see Fig. 2(c)], which leads to the positive α from Eq. (22).

Similar to the local cluster $AFD_{R,cl}$ in the T phase, there are partially ordered AFD of local clusters $AFD_{R,cl}$ and $AFD_{M,cl}$ in C phase. The average values of ω_R (respectively, ω_M) inside the $AFD_{R,cl}$ (respectively, $AFD_{M,cl}$) clusters are used as θ (respectively, ω) in the models of Eqs. (11) and (14) to analyze the entropy change. Figure 6(b) shows the isothermal entropy change computed from MC simulation [ΔS (MC)], the model in Eq. (14) [ΔS (model)] and its contribution from different terms, as a function of electric field at 450 K. Similar to the T phase, the ΔS_{field} and ΔS_{polar} are negative, ΔS_{coup} is almost zero, ΔS_{tilt} is positive and very large. Clearly, it is ΔS_{tilt} that mainly results in the inverse ECE in the C phase, similar to that in the T phase where the large positive tilting entropy change comes from the strong coupling between AFD and soft mode motions in local clusters under electric field.

IV. DISCUSSION

All the nonpolar phases of the O ($a^-a^-c^+$), T ($a^0a^0c^+$), and C ($a^0a^0a^0$) phases in CsPbI_3 possess inverse ECE, originating from the AFD (highly ordered or partly ordered) entropy change. The result of AFD entropy changes resulting in inverse ECE is different from the hypothesis in which antipolar entropy change gives rise to the inverse ECE [2,28]. In CsPbI_3 , the antipolar entropy change is almost zero in the O phase, and there is no macroscopic antipolar motion in the T and C phases. Our results of inverse ECE in the paraelectric phase of the T and C phases are in contrast with the calculations of the unified perturbation model [52] in which the paraelectric compounds possess *normal* ECE. This is because of the parameter of the AFD cluster and its coupling with soft mode, which leads to the dielectric susceptibility χ decreases with the decreasing of temperature [Fig. 2(a)], in contrast with the normal Curie-Weiss law [52].

Such inverse ECE coming from the AFD entropy change in nonpolar phases can also exist in other perovskites, including both halide and oxide perovskites. We take BaCeO_3 as an example to investigate the ECE in oxide

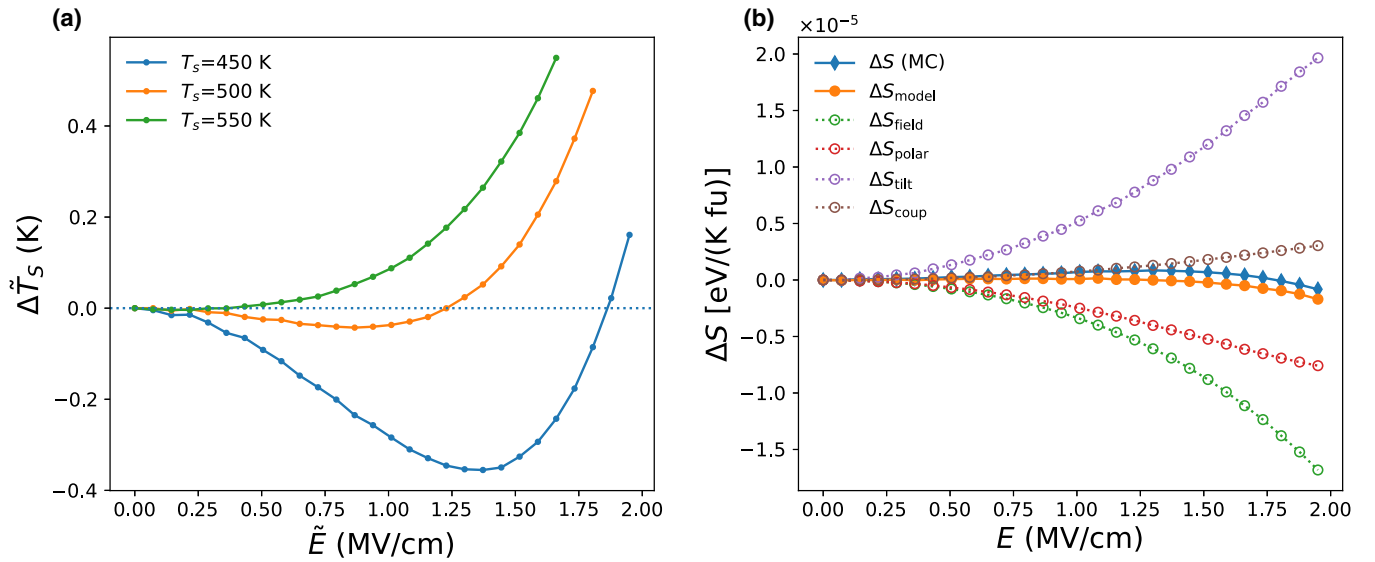


FIG. 6. Electrocaloric response in the C phase. (a) Adiabatic temperature change induced by applying electric field starting from the temperature of 450, 500, and 550 K. (b) Isothermal entropy change computed from MC simulation [ΔS (MC)], simplified model [ΔS (model), Eq. (14)] and its contribution terms, as a function of electric field at 450 K.

perovskites. As suggested in previous measurements [55,56] and first-principles-based calculations [57], BaCeO_3 possesses paraelectric $Pm\bar{3}m$ phase, nonpolar tetrahedral $I4/mcm$ phase (with AFD pattern $a^-a^0a^0$) and antipolar orthorhombic $Pbnm$ phase (with AFD pattern $a^-a^-c^+$) as the temperature decreases from 1200 K to room temperature in a monodomain form. The adiabatic temperature change are calculated for different phases of BaCeO_3 [57] as shown in Fig. 7. The structure phase is the O phase ($a^-a^-c^+$) at the starting temperature of 400 K, and the T phase ($a^-a^0a^0$) at the starting temperature of 800 K, the C phase ($a^0a^0a^0$) at the starting temperature of 1200 K. All the phases exhibit inverse ECE at certain small electric field range.

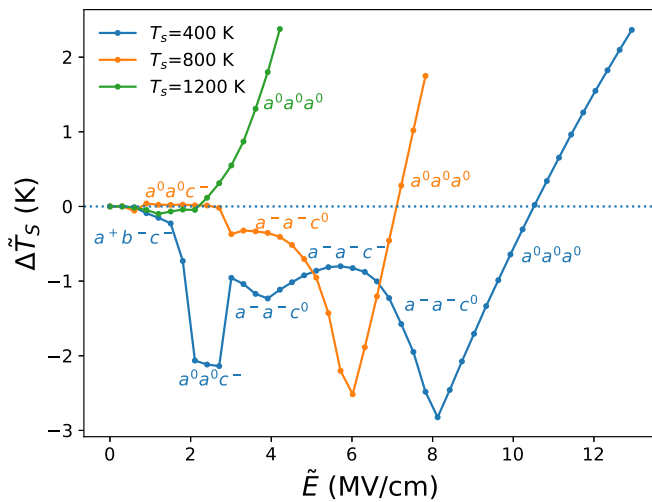


FIG. 7. Inverse ECE in BaCeO_3 . Adiabatic temperature change of BaCeO_3 as a function of electric field starting from 400 K (in $Pbnm$ O phase), 800 K (in $I4/mcm$ T phase), and 1200 K (in $Pm\bar{3}m$ C phase). The AFD patterns of structures on electric field are labeled on the corresponding curves.

Before ending the discussion, let us note the similarities and differences between the numeric methods evaluating ECE used in this work and that proposed by Pirc *et al.* [58]. Both the methods compute the temperature change in similar adiabatic processes, in which the entropy of some degrees of freedom is treated explicitly, while that of others are treated implicitly with the Equipartition theorem. The main differences are twofold. First, in the method proposed by Pirc *et al.*, the adiabatic temperature change is obtained by solving the self-consistent equation directly (see Eq. (4) in Ref. [58]), while in our method, it is obtained by tracing the isentropic lines (see Eq. (5) and the inset of Fig. 3(c)). In our method, the quantities related to the enthalpy [ΔH and $\Delta(H/T)$] (which are directly available from the effective Hamiltonian simulations) are used in the calculation of entropy change in the isothermal process [Eq. (2)] and the zero field process [Eq. (4)] to improve the numerical accuracy. Second, in Pirc *et al.*'s work, only the elementary dipolar degrees of freedom are treated explicitly using the Landau free energy model, while in our method, not only the dipolar ($\{\mathbf{u}\}$), but also the strain ($\{\mathbf{v}\}$ and η_H) and AFD ($\{\boldsymbol{\omega}\}$) degrees of freedom are treated explicitly using the first-principles-based effective Hamiltonian. Note that the AFD degrees of freedom are shown to play vital role in the inverse ECE of CsPbI_3 in the present work. As a result, while the method proposed by Pirc *et al.* provides a simple and general way to evaluate the ECE, our method makes fewer approximations by using more information from the first-principle-based effective Hamiltonian, and is expected to provide better accuracy in the context of evaluating the ECE from the effective Hamiltonian simulations.

V. SUMMARY

The novel phenomena of inverse ECE is found in a very broad range of temperature in nonpolar phases of the O, T, and

C phases for halide and oxide perovskites. These inverse ECE is induced by the octahedra AFD related entropy change under the application of electric field and by the strong coupling between AFD and polarization in the nonpolar phases. We thus expect that the presently determined inverse ECE would be measured as the important thermal control in the perovskite application in electronic, photoelectric and photovoltaic devices.

ACKNOWLEDGMENTS

X.M., Y.Y., and D.W. thank the National Key R&D Programs of China (Grants No. 2020YFA0711504 and No. 2022YFB3807601), the National Science Foundation of China (Grant No. 12274201, No. 51725203, No. 51721001, No. 52003117, and No. U1932115) and the Natural Science Foundation of Jiangsu Province (Grant No. BK20200262). We are grateful to the HPCC resources of Nanjing University for the calculations.

-
- [1] IEA, *The Future of Cooling*, Tech. Rep. (IEA, 2018).
- [2] J. Shi, D. Han, Z. Li, L. Yang, S.-G. Lu, Z. Zhong, J. Chen, Q. Zhang, and X. Qian, Electrocaloric cooling materials and devices for zero-global-warming-potential, high-efficiency refrigeration, *Joule* **3**, 1200 (2019).
- [3] X. Moya and N. D. Mathur, Caloric materials for cooling and heating, *Science* **370**, 797 (2020).
- [4] X. Moya, S. Kar-Narayan, and N. D. Mathur, Caloric materials near ferroic phase transitions, *Nat. Mater.* **13**, 439 (2014).
- [5] A. S. Mischenko, Giant electrocaloric effect in thin-film $\text{PbZr}_{0.95}\text{Ti}_{0.05}\text{O}_3$, *Science* **311**, 1270 (2006).
- [6] B. Neese, B. Chu, S.-G. Lu, Y. Wang, E. Furman, and Q. M. Zhang, Large electrocaloric effect in ferroelectric polymers near room temperature, *Science* **321**, 821 (2008).
- [7] X. Liu, Z. Wu, T. Guan, H. Jiang, P. Long, X. Li, C. Ji, S. Chen, Z. Sun, and J. Luo, Giant room temperature electrocaloric effect in a layered hybrid perovskite ferroelectric: $[(\text{CH}_3)_2\text{CHCH}_2\text{NH}_3]_2\text{PbCl}_4$, *Nat. Commun.* **12**, 5502 (2021).
- [8] V. Franco, J. Blázquez, J. Ipus, J. Law, L. Moreno-Ramírez, and A. Conde, Magnetocaloric effect: From materials research to refrigeration devices, *Prog. Mater. Sci.* **93**, 112 (2018).
- [9] J. Tušek, K. Engelbrecht, D. Eriksen, S. Dall'Olio, J. Tušek, and N. Pryds, A regenerative elastocaloric heat pump, *Nat. Energy* **1**, 16134 (2016).
- [10] B. Li, Y. Kawakita, S. Ohira-Kawamura, T. Sugahara, H. Wang, J. Wang, Y. Chen, S. I. Kawaguchi, S. Kawaguchi, K. Ohara, K. Li, D. Yu, R. Mole, T. Hattori, T. Kikuchi, S.-i. Yano, Z. Zhang, Z. Zhang, W. Ren, S. Lin, O. Sakata, K. Nakajima, and Z. Zhang, Colossal barocaloric effects in plastic crystals, *Nature (London)* **567**, 506 (2019).
- [11] R. Wang, S. Fang, Y. Xiao, E. Gao, N. Jiang, Y. Li, L. Mou, Y. Shen, W. Zhao, S. Li, A. F. Fonseca, D. S. Galvão, M. Chen, W. He, K. Yu, H. Lu, X. Wang, D. Qian, A. E. Aliev, N. Li, C. S. Haines, Z. Liu, J. Mu, Z. Wang, S. Yin, M. D. Lima, B. An, X. Zhou, Z. Liu, and R. H. Baughman, Torsional refrigeration by twisted, coiled, and supercoiled fibers, *Science* **366**, 216 (2019).
- [12] A. L. Moore and L. Shi, Emerging challenges and materials for thermal management of electronics, *Mater. Today* **17**, 163 (2014).
- [13] P. Ball, Computer engineering: Feeling the heat, *Nature (London)* **492**, 174 (2012).
- [14] A. Grünebohm, Y.-B. Ma, M. Marathe, B.-X. Xu, K. Albe, C. Kalcher, K.-C. Meyer, V. V. Shvartsman, D. C. Lupascu, and C. Ederer, Origins of the inverse electrocaloric effect, *Energy Technol.* **6**, 1491 (2018).
- [15] I. Ponomareva and S. Lisenkov, Bridging the Macroscopic and Atomistic Descriptions of the Electrocaloric Effect, *Phys. Rev. Lett.* **108**, 167604 (2012).
- [16] V. Basso, J.-F. Gerard, and S. Pruvost, Doubling the electrocaloric cooling of poled ferroelectric materials by bipolar cycling, *Appl. Phys. Lett.* **105**, 052907 (2014).
- [17] Y.-B. Ma, N. Novak, J. Koruza, T. Yang, K. Albe, and B.-X. Xu, Enhanced electrocaloric cooling in ferroelectric single crystals by electric field reversal, *Phys. Rev. B* **94**, 100104(R) (2016).
- [18] M. Marathe, D. Renggli, M. Sanliyalp, M. O. Karabasov, V. V. Shvartsman, D. C. Lupascu, A. Grünebohm, and C. Ederer, Electrocaloric effect in BaTiO_3 at all three ferroelectric transitions: Anisotropy and inverse caloric effects, *Phys. Rev. B* **96**, 014102 (2017).
- [19] C. Cazorla and J. Íñiguez, Giant direct and inverse electrocaloric effects in multiferroic thin films, *Phys. Rev. B* **98**, 174105 (2018).
- [20] X. Moya, E. Stern-Taulats, S. Crossley, D. González-Alonso, S. Kar-Narayan, A. Planes, L. Mañosa, and N. D. Mathur, Giant electrocaloric strength in single-crystal BaTiO_3 , *Adv. Mater.* **25**, 1360 (2013).
- [21] R. Gao, X. Shi, J. Wang, G. Zhang, and H. Huang, Designed giant room-temperature electrocaloric effects in metal-free organic perovskite $[\text{MDABCO}](\text{NH}_4)_3$ by phase-field simulations, *Adv. Funct. Mater.* **31**, 2104393 (2021).
- [22] B. Nair, T. Usui, S. Crossley, S. Kurdi, G. G. Guzmán-Verri, X. Moya, S. Hirose, and N. D. Mathur, Large electrocaloric effects in oxide multilayer capacitors over a wide temperature range, *Nature (London)* **575**, 468 (2019).
- [23] A. Torelló, P. Lheritier, T. Usui, Y. Nouchokgwe, M. Gérard, O. Bouton, S. Hirose, and E. Defay, Giant temperature span in electrocaloric regenerator, *Science* **370**, 125 (2020).
- [24] X. Qian, D. Han, L. Zheng, J. Chen, M. Tyagi, Q. Li, F. Du, S. Zheng, X. Huang, S. Zhang, J. Shi, H. Huang, X. Shi, J. Chen, H. Qin, J. Bernholc, X. Chen, L.-Q. Chen, L. Hong, and Q. M. Zhang, High-entropy polymer produces a giant electrocaloric effect at low fields, *Nature (London)* **600**, 664 (2021).
- [25] R. Ma, Z. Zhang, K. Tong, D. Huber, R. Kornbluh, Y. S. Ju, and Q. Pei, Highly efficient electrocaloric cooling with electrostatic actuation, *Science* **357**, 1130 (2017).
- [26] M.-D. Li, X.-Q. Shen, X. Chen, J.-M. Gan, F. Wang, J. Li, X.-L. Wang, and Q.-D. Shen, Thermal management of chips by a device prototype using synergistic effects of 3-D heat-conductive network and electrocaloric refrigeration, *Nat. Commun.* **13**, 5849 (2022).

- [27] G. Zhang, Q. Li, H. Gu, S. Jiang, K. Han, M. R. Gadinski, M. A. Haque, Q. Zhang, and Q. Wang, Ferroelectric polymer nanocomposites for room-temperature electrocaloric refrigeration, *Adv. Mater.* **27**, 1450 (2015).
- [28] W. Geng, Y. Liu, X. Meng, L. Bellaiche, J. F. Scott, B. Dkhil, and A. Jiang, Giant negative electrocaloric effect in antiferroelectric la-doped $\text{Pb}(\text{ZrTi})\text{O}_3$ thin films near room temperature, *Adv. Mater.* **27**, 3165 (2015).
- [29] P. Vales-Castro, R. Faye, M. Vellvehi, Y. Nouchokgwe, X. Perpiñà, J. M. Caicedo, X. Jordà, K. Roleder, D. Kajewski, A. Perez-Tomas, E. Defay, and G. Catalan, Origin of large negative electrocaloric effect in antiferroelectric PbZrO_3 , *Phys. Rev. B* **103**, 054112 (2021).
- [30] J. Peräntie, J. Hagberg, A. Uusimäki, and H. Jantunen, Electric-field-induced dielectric and temperature changes in a $\langle 011 \rangle$ -oriented $\text{Pb}(\text{Mg}_{1/3}\text{Nb}_{2/3}\text{O}_3)$ - PbTiO_3 single crystal, *Phys. Rev. B* **82**, 134119 (2010).
- [31] Y. Bai, G.-P. Zheng, and S.-Q. Shi, Abnormal electrocaloric effect of $\text{Na}_{0.5}\text{Bi}_{0.5}\text{TiO}_3$ - BaTiO_3 lead-free ferroelectric ceramics above room temperature, *Mater. Res. Bull.* **46**, 1866 (2011).
- [32] N. Fan, J. Íñiguez, L. Bellaiche, and B. Xu, Origin of negative electrocaloric effect in pnma-type antiferroelectric perovskites, *Phys. Rev. B* **106**, 224107 (2022).
- [33] H. J. Snaith, Perovskites: the emergence of a new era for low-cost, high-efficiency solar cells, *J. Phys. Chem. Lett.* **4**, 3623 (2013).
- [34] L. Protesescu, S. Yakunin, M. I. Bodnarchuk, F. Krieg, R. Caputo, C. H. Hendon, R. X. Yang, A. Walsh, and M. V. Kovalenko, Nanocrystals of cesium lead halide perovskites (CsPbX_3 , $X = \text{Cl, Br, and I}$): novel optoelectronic materials showing bright emission with wide color gamut, *Nano Lett.* **15**, 3692 (2015).
- [35] A. Swarnkar, A. R. Marshall, E. M. Sanehira, B. D. Chernomordik, D. T. Moore, J. A. Christians, T. Chakrabarti, and J. M. Luther, Quantum dot-induced phase stabilization of α - CsPbI_3 perovskite for high-efficiency photovoltaics, *Science* **354**, 92 (2016).
- [36] L. Chen, B. Xu, Y. Yang, and L. Bellaiche, Macroscopic and microscopic structures of cesium lead iodide perovskite from atomistic simulations, *Adv. Funct. Mater.* **30**, 1909496 (2020).
- [37] W. Zhong, D. Vanderbilt, and K. M. Rabe, First-principles theory of ferroelectric phase transitions for perovskites: The case of BaTiO_3 , *Phys. Rev. B* **52**, 6301 (1995).
- [38] S. Prosandeev, D. Wang, A. R. Akbarzadeh, B. Dkhil, and L. Bellaiche, Field-Induced Percolation of Polar Nanoregions in Relaxor Ferroelectrics, *Phys. Rev. Lett.* **110**, 207601 (2013).
- [39] Z. Jiang, S. Prokhorenko, S. Prosandeev, Y. Nahas, D. Wang, J. Íñiguez, E. Defay, and L. Bellaiche, Electrocaloric effects in the lead-free $\text{Ba}(\text{Zr, Ti})\text{O}_3$ relaxor ferroelectric from atomistic simulations, *Phys. Rev. B* **96**, 014114 (2017).
- [40] B. Xu, J. I. niguez, and L. Bellaiche, Designing lead-free antiferroelectrics for energy storage, *Nat. Commun.* **8**, 15682 (2017).
- [41] X. Ma, Y. Yang, L. Bellaiche, and D. Wu, Large electrocaloric response via percolation of polar nanoregions, *Phys. Rev. B* **105**, 054104 (2022).
- [42] A. R. Akbarzadeh, S. Prosandeev, E. J. Walter, A. Al-Barakaty, and L. Bellaiche, Finite-Temperature Properties of $\text{Ba}(\text{Zr, Ti})\text{O}_3$ Relaxors from First Principles, *Phys. Rev. Lett.* **108**, 257601 (2012).
- [43] Z. Jiang, B. Xu, S. Prosandeev, Y. Nahas, S. Prokhorenko, J. Íñiguez, and L. Bellaiche, Electrocaloric effects in multiferroics, *Phys. Rev. B* **103**, L100102 (2021).
- [44] S. Duane, A. Kennedy, B. J. Pendleton, and D. Roweth, Hybrid monte carlo, *Phys. Lett. B* **195**, 216 (1987).
- [45] B. Mehlig, D. W. Heermann, and B. M. Forrest, Hybrid Monte Carlo method for condensed-matter systems, *Phys. Rev. B* **45**, 679 (1992).
- [46] S. Prokhorenko, K. Kalke, Y. Nahas, and L. Bellaiche, Large scale hybrid Monte Carlo simulations for structure and property prediction, *npj Comput. Mater.* **4**, 80 (2018).
- [47] N. Metropolis, A. W. Rosenbluth, M. N. Rosenbluth, A. H. Teller, and E. Teller, Equation of state calculations by fast computing machines, *J. Chem. Phys.* **21**, 1087 (1953).
- [48] U. V. Waghmare, E. J. Cockayne, and B. P. Burton, Ferroelectric phase transitions in nano-scale chemically ordered $\text{PbSc}_{0.5}\text{Nb}_{0.5}\text{O}_3$ using a first-principles model hamiltonian, *Ferroelectrics* **291**, 187 (2003).
- [49] T. Nishimatsu, U. V. Waghmare, Y. Kawazoe, and D. Vanderbilt, Fast molecular-dynamics simulation for ferroelectric thin-film capacitors using a first-principles effective Hamiltonian, *Phys. Rev. B* **78**, 104104 (2008).
- [50] A. M. Glazer, The classification of tilted octahedra in perovskites, *Acta Crystallogr. Sect. B* **28**, 3384 (1972).
- [51] A. Marronnier, G. Roma, S. Boyer-Richard, L. Pedesseau, J.-M. Jancu, Y. Bonnassieux, C. Katan, C. C. Stoumpos, M. G. Kanatzidis, and J. Even, Anharmonicity and disorder in the black phases of cesium lead iodide used for stable inorganic perovskite solar cells, *ACS Nano* **12**, 3477 (2018).
- [52] M. Graf and J. Íñiguez, A unified perturbative approach to electrocaloric effects, *Commun. Mater.* **2**, 60 (2021).
- [53] S. Prosandeev, D. Wang, and L. Bellaiche, Properties of Epitaxial Films Made of Relaxor Ferroelectrics, *Phys. Rev. Lett.* **111**, 247602 (2013).
- [54] X. Wang, K. Patel, S. Prosandeev, Y. Zhang, C. Zhong, B. Xu, and L. Bellaiche, Finite-temperature dynamics in cesium lead iodide halide perovskite, *Adv. Funct. Mater.* **31**, 2106264 (2021).
- [55] Z. Zhang, J. Koppensteiner, W. Schranz, J. B. Betts, A. Migliori, and M. A. Carpenter, Microstructure dynamics in orthorhombic perovskites, *Phys. Rev. B* **82**, 014113 (2010).
- [56] S.-Y. Cheng, N.-J. Ho, and H.-Y. Lu, Phase-transformation-induced twinning in orthorhombic BaCeO_3 , *J. Am. Ceram. Soc.* **91**, 2298 (2008).
- [57] Y. Yang, H. Xiang, and L. Bellaiche, Revisiting structural phases in some perovskites: The case of BaCeO_3 , *Phys. Rev. B* **104**, 174102 (2021).
- [58] R. Pirc, Z. Kutnjak, R. Blinc, and Q. M. Zhang, Electrocaloric effect in relaxor ferroelectrics, *J. Appl. Phys.* **110**, 074113 (2011).